ADVANCED MATERIALS
www.advmat.de

Symmetry Control of Unconventional Spin–Orbit Torques in IrO_2

*Michael Patton, Gautam Gurung, Ding-Fu Shao, Gahee Noh, Joseph A. Mittelstaedt, Marcel Mazur, Jong-Woo Kim, Philip J. Ryan, Evgeny Y. Tsymbal, Si-Young Choi, Daniel C. Ralph, Mark S. Rzchowski, Tianxiang Nan, and Chang-Beom Eom**

Spin–orbit torques generated by a spin current are key to magnetic switching in spintronic applications. The polarization of the spin current dictates the direction of switching required for energy-efficient devices. Conventionally, the polarizations of these spin currents are restricted to be along a certain direction due to the symmetry of the material allowing only for efficient in-plane magnetic switching. Unconventional spin–orbit torques arising from novel spin current polarizations, however, have the potential to switch other magnetization orientations such as perpendicular magnetic anisotropy, which is desired for higher density spintronic-based memory devices. Here, it is demonstrated that low crystalline symmetry is not required for unconventional spin–orbit torques and can be generated in a nonmagnetic high symmetry material, iridium dioxide (IrO_2), using epitaxial design. It is shown that by reducing the relative crystalline symmetry with respect to the growth direction large unconventional spin currents can be generated and hence spin–orbit torques. Furthermore, the spin polarizations detected in (001), (110), and (111) oriented IrO_2 thin films are compared to show which crystal symmetries restrict unconventional spin transport. Understanding and tuning unconventional spin transport generation in high symmetry materials can provide a new route towards energy-efficient magnetic switching in spintronic devices.

1. Introduction

Magnetic manipulation via spin–orbit torques (SOTs) generated by spin currents are at the heart of spintronic devices and have been heavily studied in materials hosting charge-to-spin conversion mechanisms such as the spin Hall effect (SHE).[1–3] In heavy metal/ferromagnetic bilayers for spintronic devices, magnetic switching via spin currents requires the spins to be polarized along a certain direction. In high symmetry materials the spin polarization of the spin currents generated via the SHE is restricted to be orthogonal to the spin flow and charge current directions which limits magnetization switching in one direction. Lower symmetry materials, however, can host additional spin currents with polarizations aligned along the charge current direction or aligned along the spin flow direction. These unconventional spin currents have been observed at ferromagnetic interfaces due to spin scattering,[4,5] antiferromagnetic materials due to the low magnetic symmetry,[6–10] and in low symmetry transition-metal dichalcogenide

M. Patton, C.-B. Eom
Department of Materials Science and Engineering
University of Wisconsin-Madison
Madison, WI 53706, USA
E-mail: eom@engr.wisc.edu

G. Gurung, D.-F. Shao, E. Y. Tsymbal
Department of Physics and Astronomy & Nebraska Center for Materials and Nanoscience
University of Nebraska
Lincoln, NE 68588, USA

The ORCID identification number(s) for the author(s) of this article can be found under https://doi.org/10.1002/adma.202301608

DOI: 10.1002/adma.202301608

G. Noh, S.-Y. Choi
Department of Materials Science and Engineering
Pohang University of Science and Technology
Pohang, Gyeongbuk 37673, Republic of Korea

J. A. Mittelstaedt, M. Mazur, D. C. Ralph
Cornell University
Ithaca, NY 14853, USA

J.-W. Kim, P. J. Ryan
X-Ray Science Division
Argonne National Laboratory
Argonne, IL 60439, USA

P. J. Ryan
School of Physical Sciences
Dublin City University
Dublin 9, Ireland

S.-Y. Choi
Center for Van der Waals Quantum Solids
Institute for Basic Science (IBS)
Pohang 37673, Republic of Korea

(TMD)/ferromagnetic bilayers and in $L1_1$-ordered CuPt/CoPt bilayers.[11–17] Most of the studies to date that show unconventional SOTs occur in systems that have low symmetry throughout the bulk of the material, whereas in high symmetry materials, unconventional spin transport is typically forbidden due to crystal symmetries relative to the flow of charge current (J_c), spin current (J_s), and spin polarization (S). Here, we show that unconventional spin transport in high symmetry materials can be realized by manipulating the crystal structure via epitaxial design to lower the symmetry relative to J_c, J_s, and S.

Rutile iridium dioxide (IrO_2), a nonmagnetic metallic oxide, has been shown to have a large spin-charge conversion efficiency and high electrical conductivity making this material promising for spintronic applications.[18–22] Only conventional spin–orbit torques have been observed in IrO_2 in previous studies of polycrystalline films and high symmetry orientations such as (001) crystalline films[18,19] due to combinations of symmetry elements that forbid unconventional SOTs. However, lower symmetry orientations can be achieved by utilizing the structural anisotropy due to tetragonality of the rutile crystal structure. IrO_2 in lower symmetry orientations where the crystal symmetry relative to the growth direction is reduced has yet to be studied and could result in unconventional spin transport similar to TMD/ferromagnetic bilayers that support unconventional SOTs.[13] Other studies have compared different crystallographic orientations in IrO_2 and Pt epitaxial films, however, the primary focus of these studies were to show the orientational and strain effects on the conventional SOTs.[19,23,24] Studying the unconventional SHE in different relative symmetry states in a material such as IrO_2 would refine the search for materials with unconventional spin transport and give insight into which symmetries restrict this novel property for next generation spintronic devices.

Here we show unconventional SOT generation in IrO_2 based devices by controlling the relative crystal orientation of IrO_2 using epitaxial design. The SOTs in IrO_2 were studied for (001), (110), and (111) oriented thin films along different in-plane crystallographic directions using spin-torque ferromagnetic resonance (ST-FMR), which agree well with our theoretical calculations. We find unconventional in-plane SOTs for both the (110) and (111) oriented films as well as out-of-plane unconventional SOTs in the (111) orientation. These results demonstrate how unconventional spin transport can be observed even in higher symmetry materials expanding our understanding of crystal symmetries that allow for unconventional SOTs which could lead to more efficient spintronic devices using any arbitrary magnetization direction.

S.-Y. Choi
Semiconductor Engineering
Pohang University of Science and Technology (POSTECH)
Pohang 37673, Republic of Korea

D. C. Ralph
Kavli Institute at Cornell for Nanoscale Science
Ithaca, NY 14853, USA

M. S. Rzchowski
Department of Physics
University of Wisconsin-Madison
Madison, WI 53706, USA

T. Nan
School of Integrated Circuits and Beijing National Research Center for Information Science and Technology (BNRist)
Tsinghua University
Beijing 100084, China

2. Results and Discussion

The spin Hall conductivity (SHC) denoted as σ_{jk}^{i} (where i is the spin polarization direction, j is the spin flow direction, and k is the charge current direction) is a third order tensor calculated from the spin Berry curvature of a material.[22,25] The symmetry of a material restricts which SHC elements can have nonzero values leading to high symmetry materials only hosting conventional SHC where the spin polarization direction, charge current direction, and spin flow direction are all orthogonal. Materials that have lower intrinsic crystalline symmetry such as TMDs can allow for spin polarizations that are typically not observed in high symmetry spin source materials. WTe_2, for example, only hosts one mirror plane perpendicular to the surface orientation, leading to unconventional out-of-plane spin currents.[13]

We have selected IrO_2 as our high symmetry model system to study the relationship between symmetry operations and unconventional SOTs. IrO_2 (space group $P4_2/mnm$ No. 136) has a tetragonal rutile crystal structure with mirror symmetry (m) along the (001), (110), and (1-10) planes, twofold rotational symmetries along (C_2) [001], [110], and [1-10], and nonsymmorphic symmetries that include a fourfold rotational screw axis ($\tilde{C}_4$) along [001] and glide mirror planes along the ($\tilde{m}$) (100) and (010) planes. Combinations of these symmetry elements in high symmetry orientations forbid any unconventional SOTs arising from the bulk of the material. Considering the (001) orientation, for example, both the in-plane unconventional SHCs, i.e., σ_{zx}^{y} or σ_{zy}^{y}, and the out-of-plane unconventional SHCs, i.e., σ_{zx}^{z} or σ_{zy}^{z}, are not allowed, due to the existence of the (001), (110), and (1-10) mirror planes, and the fourfold screw axis along [001], as shown in **Figure 1**a. In the (110) orientation, similar to the (001) orientation, no out-of-plane unconventional SHCs would be expected due to the (110) mirror plane. Due to the crystalline anisotropy as a result of the tetragonality of the rutile structure, the in-plane unconventional SHCs are no longer restricted due to the combination of out-of-plane and in-plane mirror symmetries seen in Figure 1b. These unconventional in-plane SHCs would, however, vanish when charge current is applied along the high symmetry directions [001] and [1-10] which was seen in a previous study.[19] Symmetry analysis of the SHC (see the Experimental Section) indicate a $\sin(2\psi)$ dependance of the in-plane unconventional SOTs as current is applied at an angle ψ away from the (001) mirror plane. Lastly, considering a low symmetry orientation in IrO_2 (111), there is only one in-plane mirror (1-10) plane parallel to the out-of-plane spin currents, as shown in Figure 1c. The (1-10) mirror plane restricts any z-polarized out-of-plane spin current with charge current applied parallel to the mirror plane, however, current applied perpendicular should allow for out-of-plane unconventional SHCs. Likewise, in-plane unconventional SHCs are restricted with current applied parallel and perpendicular to the (1-10) mirror plane, however, these in-plane SHCs should be nonzero when charge

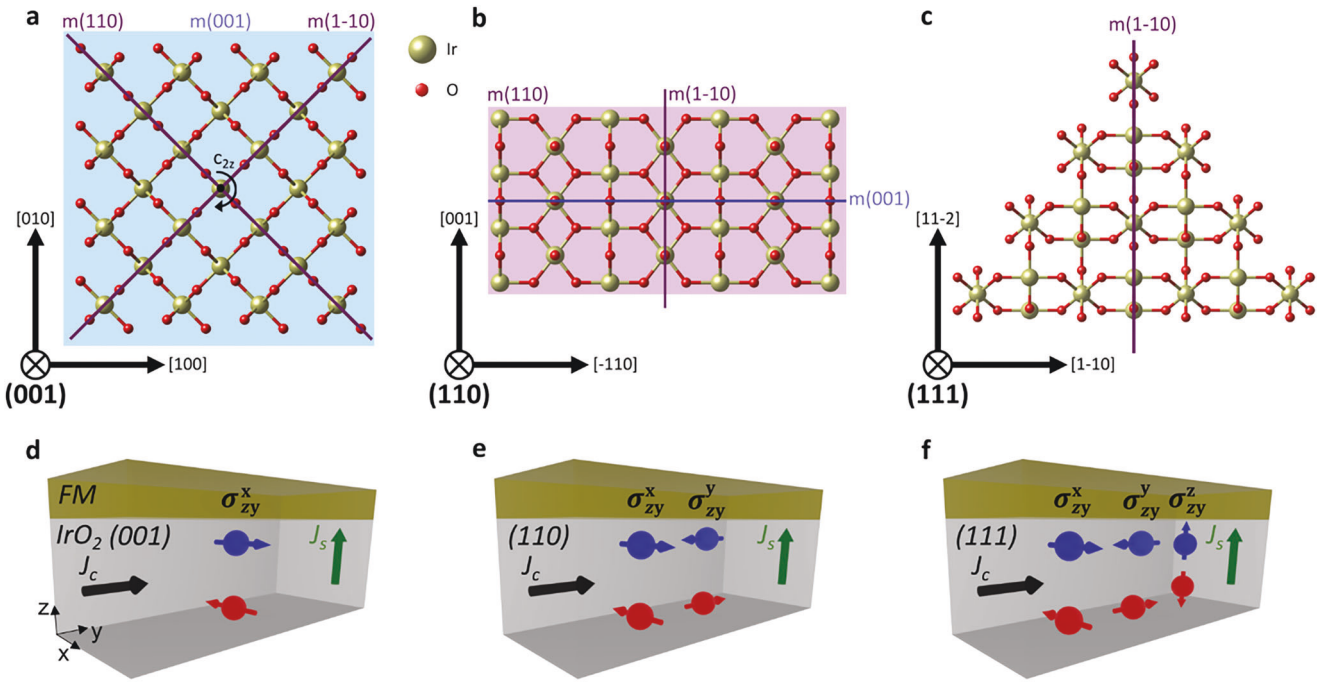

Figure 1. Epitaxial design for unconventional SOTs in IrO_2. a–c) The IrO_2 (001), (110), and (111) projections of the rutile crystal structure with crystal symmetries. d–f) The allowed spin Hall conductivity tensors for the (001), (110), and (111) orientations for a resulting spin current (J_s) in the *z*-directions generated from a charge current (J_c) applied in the *y* direction.

current is applied at some in-plane angle between 0° and 90° with respect to the mirror plane. With these unconventional SHCs, the low symmetric oriented IrO_2 film can be used as a promising spin source to exert unconventional SOTs on the adjacent ferromagnetic layer.

Epitaxial IrO_2 thin films were grown on single-crystal 5 mm x 5 mm x 1 mm TiO_2 (001), 5 mm x 5 mm x 0.5 mm (110), and 5 mm x 5 mm x 0.5 mm (111) oriented substrates via RF magnetron sputtering with a ferromagnetic Permalloy (Py) overlayer used as the spin detector for the spintronic measurements. Fully epitaxial IrO_2 samples were achieved for each orientation and confirmed with high resolution X-ray diffraction (HRXRD) seen in **Figure 2**a–c for Py(8 nm)/IrO_2(10 nm)/TiO_2(001), Py(8 nm)/IrO_2(7.5 nm)/TiO_2(110), and Py(8 nm)/IrO_2(7.5 nm)/TiO_2(111) samples. The HRXRD scans show the IrO_2 film peak accompanied by Kiessig fringes, confirming the high quality of IrO_2 growth. A wider range out-of-plane scan was also performed to confirm single phase was achieved for each orientation shown in Figure S1a in the Supporting Information. Additionally, reciprocal space maps (RSMs) were performed on in-plane peaks for each orientation to determine the in-plane epitaxial strain shown in Figure S1b–f in the Supporting Information. Scanning transmission electron microscopy (STEM) seen in Figure 2d–f was done for each orientation which demonstrates the sharp interface between IrO_2 and Py and between IrO_2 and TiO_2, which helps rule out any extrinsic effects that may contribute to the SOTs. Geometric phase analysis (GPA) was used to determine the strain states along two orthogonal in-plane directions for each orientation shown in Figures S2–S4 in the Supporting Information. To determine the SHC for (001), (110), and (111) oriented IrO_2, samples were patterned into 50 µm × 100 µm microstrips with a ground-source-ground electrode pattern for spin-torque ferromagnetic resonance (ST-FMR) measurements seen in Figure 2g. Angular ST-FMR measurements[26] were performed to determine the SHC for IrO_2 films where a magnetic field is swept in-plane at different angles with respect to the microstrip while applying a microwave current I_{rf} (see the Experimental Section).

Conventionally, torques generated from Oersted fields acting on the magnetization are in the form of $m \times y$ where y is an in-plane direction perpendicular to the charge current direction x (Figure 2h), resulting in a field-like torque ($\tau_\perp$). In addition to the out-of-plane torques, spin currents resulting from the SHE (or other spin generating effects) can also generate torques in the form of $m \times (m \times y)$ resulting in a damping-like torque ($\tau_\parallel$).[27] The out-of-plane ($\tau_\perp$) and the in-plane ($\tau_\parallel$) torques are proportional to the mixing voltage V_{mix} as the ferromagnetic layer goes through its resonance condition which can be fitted as a sum of a symmetric and an antisymmetric Lorentzian

$$V_{mix,S} = -\frac{I_{rf}}{2}\left(\frac{dR}{d\varphi_M}\right)\frac{1}{\alpha\left(2\mu_0 H_{FMR} + \mu_0 M_{eff}\right)}\tau_\parallel \quad (1)$$

$$V_{mix,A} = -\frac{I_{rf}}{2}\left(\frac{dR}{d\varphi_M}\right)\frac{\sqrt{1 + M_{eff}/H_{FMR}}}{\alpha\left(2\mu_0 H_{FMR} + \mu_0 M_{eff}\right)}\tau_\perp \quad (2)$$

Where I_{rf} is the microwave current, R is the resistance of the device, φ_M is the magnetization angle with respect to the applied

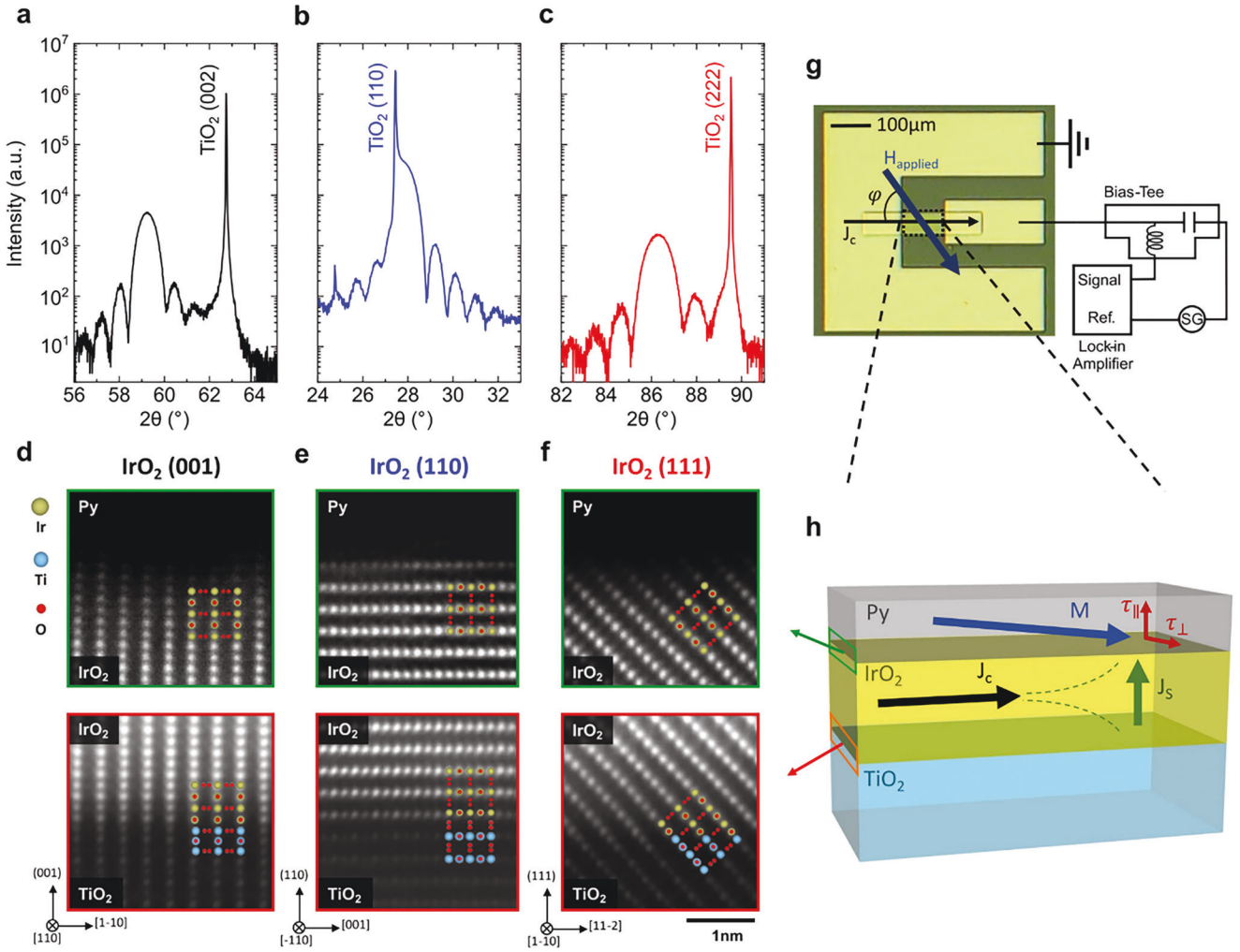

Figure 2. Film characterization and ST-FMR device schematic. a–c) Out-of-plane XRD showing epitaxial growth of IrO_2 on TiO_2 for the (001), (110), and (111) orientations. d–f) High-angle annular dark-field (HAADF)-STEM images of Py/IrO_2 and IrO_2/TiO_2 interfaces for the (001), (110), and (111) orientations with simulated unit cell. g) Schematic showing device and measurement geometry for ST-FMR measurements and h, schematic showing external applied field and resulting field-like and damping like torques in the ST-FMR measurements.

current, α is the Gilbert damping coefficient, $\mu_0 H_{FMR}$ is the resonance field, and $\mu_0 M_{eff}$ is the effective magnetization. Figure S6 in the Supporting Information shows a typical ST-FMR lineshape for IrO_2 (111), the extracted Gilbert damping coefficient and resonance field for each orientation by fitting the ST-FMR lineshape to Equations (1) and (2), microwave current calibration, and the anisotropic magnetoresistance (AMR).

To quantitatively determine all torque contributions, ST-FMR measurements were performed as a function of applied in-plane magnetic field angle (φ). In conventional heavy-metal/ferromagnetic bilayers the AMR of Py ($\frac{dR}{d\varphi_M}$) has an angular dependance proportional to $\sin(2\varphi_M) \approx \sin(2\varphi)$ and the out-of-plane ($\tau_\perp$) and the in-plane ($\tau_\parallel$) torques are proportional to $\cos(\varphi)$ resulting in the $V_{mix,S}$ and $V_{mix,A}$ being in the form of $\sin(2\varphi)\cos(\varphi)$. Additional unconventional torques that have different spin polarization directions, however, can contribute to the angular dependance resulting in a more general form, with

$$\tau_\parallel = \tau_{x,AD} \sin(\varphi) + \tau_{y,AD} \cos(\varphi) + \tau_{z,FL} \quad (3)$$

$$\tau_\perp = \tau_{x,FL} \sin(\varphi) + \tau_{y,FL} \cos(\varphi) + \tau_{z,AD} \quad (4)$$

so that $V_{mix,S}$ and $V_{mix,A}$ can then be expressed in the form of $\sin(2\varphi)(\tau_{x,AD}\sin(\varphi) + \tau_{y,AD}\cos(\varphi) + \tau_{z,FL})$ and $\sin(2\varphi)(\tau_{x,FL}\sin(\varphi) + \tau_{y,FL}\cos(\varphi) + \tau_{z,AD})$, respectively.

Figure 3 shows the angular dependance of $V_{mix,S}$ and $V_{mix,A}$ for Py(8 nm)/IrO_2(10 nm)/TiO_2(001), Py(8 nm)/IrO_2(7.5 nm)/TiO_2(110), and Py(8 nm)/IrO_2(7.5 nm)/TiO_2(111) samples for fixed directions of applied current as illustrated in the insets. The experimental angular ST-FMR data was fitted using the same $V_{mix,S}$ and $V_{mix,A}$ equations for each orientation to determine τ_x, τ_y, and τ_z. For

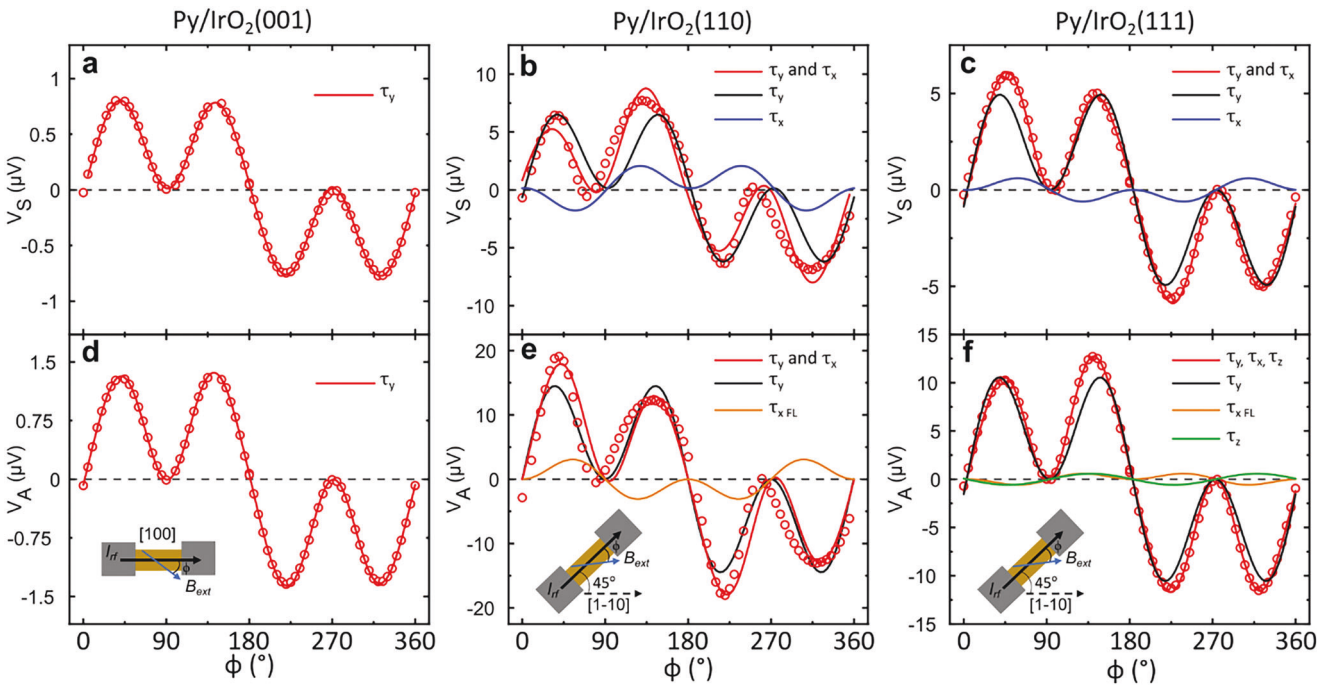

Figure 3. Angular ST-FMR results for (001), (110), and (111) IrO_2. a) Symmetric component of the mixing voltage V_s from angular ST-FMR measurements for Py(8 nm)/IrO_2(10 nm)/TiO_2(001) with the in-set showing the current I_{rf} direction along the [100] direction while the applied external field B_{ext} is rotated with respect to I_{rf} by some angle φ. Fitting the raw data with combined τ_x, τ_y, and τ_z, (001) oriented IrO_2 only shows contributions from τ_y. b) V_s for Py(8 nm)/IrO_2(7.5 nm)/TiO_2(110) as I_{rf} is applied 45° rotated in-plane from the [1-10] direction, showing contributions from conventional τ_y and unconventional in-plane τ_x. c) V_s for Py(8 nm)/IrO_2(7.5 nm)/TiO_2(111) as I_{rf} is applied 45° rotated in-plane from the [1-10] direction, showing contributions from conventional τ_y and unconventional in-plane τ_x. d) Antisymmetric component V_A for IrO_2 (001) showing contributions from conventional τ_y. e) V_A for IrO_2 (110) showing contributions from conventional τ_y and a field-like $\tau_{x\,FL}$. f) V_A for IrO_2 (111) showing contributions from conventional τ_y, field-like $\tau_{x\,FL}$, and unconventional out-of-plane τ_z.

the (001) orientation, we only find τ_y conventional torque contributions to the angular dependance for both $V_{mix,S}$ and $V_{mix,A}$, whereas the (110) and (111) orientations require additional torque components to fit the raw data. Looking at the $V_{mix,S}$ in Figure 3b,c, we find contributions from in-plane conventional τ_y spin torques (perpendicular to the charge current direction), and in-plane unconventional τ_x spin torques (aligned along the charge current direction) for both the (110) and (111) oriented films. Looking at the $V_{mix,A}$ in Figure 3e,f for the (110) and (111) oriented samples, we find a contribution from a field-like torque along the charge current direction $\tau_{x\,FL}$ in addition to the conventional τ_y torque. The field-like $\tau_{x\,FL}$ torque is likely an extrinsic mechanism caused by a small transverse current along the y direction due to anisotropic resistance and not an intrinsic unconventional torque which is discussed in more detail in Note S5 and Figure S10 in the Supporting Information. The (111) orientation also shows a contribution from out-of-plane spin polarized torques, τ_z, which was not detected in the (001) and (110) orientations. The differences between the (110) and (111) oriented $V_{mix,A}$ signal can be seen when looking at the peak height difference at 45°, 135°, 225°, and 315°. In Figure 3e for the (110) for example, the difference in peak heights follows a sin (2φ)sin (φ) angular dependance which corresponds to the $\tau_{x,FL}$. On the other hand, in Figure 3f for the (111) the difference in peak heights at 45° and 135° along with minimal peak height difference at 225° and 315° indicate contributions from a sin (2φ)sin (φ) angular dependance, corresponding to the $\tau_{x,FL}$, and a sin (2φ) angular dependance, corresponding a τ_z. Additionally, higher harmonic angular dependencies were observed and included for better fittings in the (110) and (111) orientation. These higher harmonics can be explained as due to magnetic anisotropy of the Py overlayer as detailed in the Note S4 and Figure S7 in the Supporting Information. Again, like the field-like $\tau_{x\,FL}$ torque, the higher harmonic contributions are likely due to an extrinsic effect not related to the intrinsic unconventional SOTs discussed throughout the text. The conventional SHC has a value of $\sigma^{y}_{zx} = 116\pm 1$ ($10^3\hbar/2e(\Omega\ m)^{-1}$) for the (111) oriented films, 180 ± 4 ($10^3\hbar/2e(\Omega\ m)^{-1}$) for the (001) oriented films, and 114 ± 8 ($10^3\hbar/2e(\Omega\ m)^{-1}$) for the (110) oriented films. The unconventional SOTs for (110) and (111) were fully characterized as a function of the in-plane angular dependance.

The unconventional SHCs obtained in Py(8 nm)/IrO_2(7.5 nm)/TiO_2(110) and Py(8 nm)/IrO_2(7.5 nm)/TiO_2(111) samples are dependent on the in-plane current direction with respect to the crystallographic axes due to symmetry operations. Theoretical calculations predict σ^{x}_{zx} to be proportional to sin(2ψ) for both (111) and (110) and σ^{z}_{zx} to be proportional to cos(ψ) for (111) where ψ is the angle between the applied current and the in-plane [−110] crystallographic axis shown in **Figure 4**a,b. The in-plane angular dependance of J_c for σ^{x}_{zx} for both the (110) and the (111)

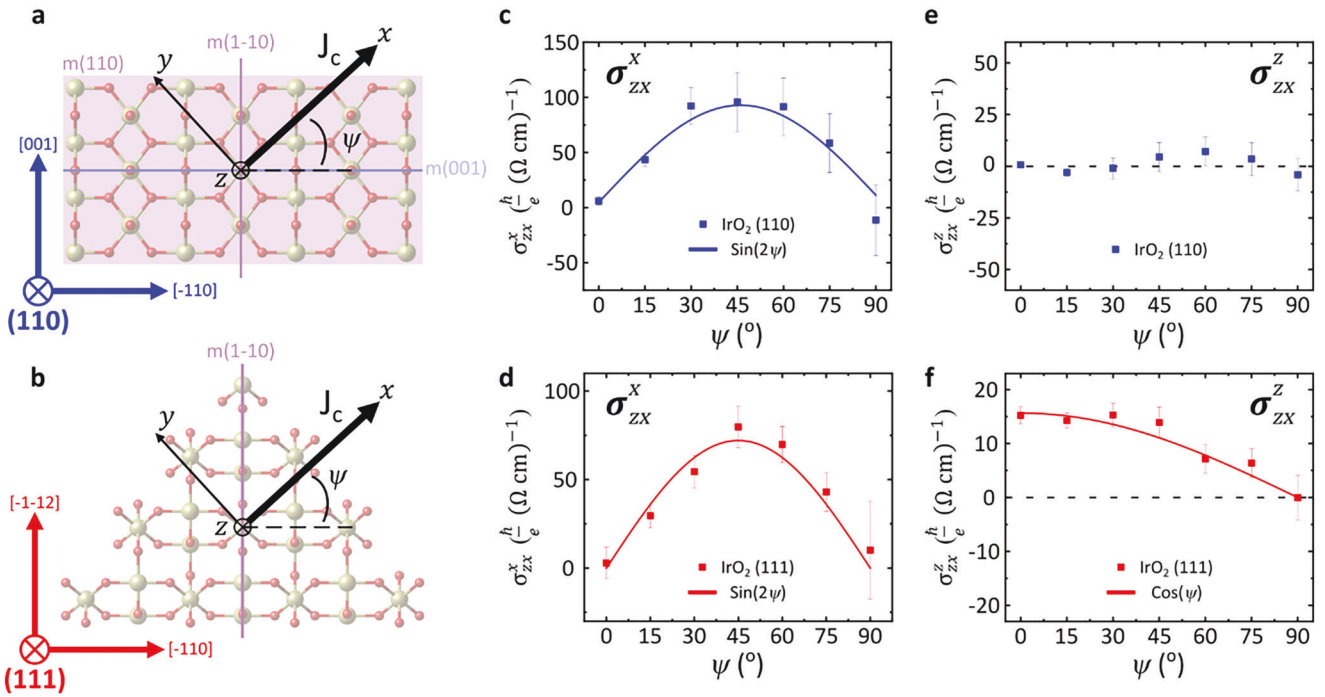

Figure 4. In-plane crystallographic dependance on unconventional SHCs a,b) IrO_2 (110) and (111) projections where $\psi = 0^o$ when charge current J_c is applied along the [−110] direction for both orientations. c–f) In-plane and out-of-plane unconventional SHCs for the (110) and (111) orientation where each data point (red square) are determined from the angular ST-FMR done at 7 GHz and 10 dBm on a device angled ψ away from the [−110] crystallographic axis compared with the theoretical calculations (black dashed line). The error bars seen in (c)–(f) represent the estimated standard deviations calculated using error propagation from the least-square fitting procedure used to determine the torque contributions from Equation 3 and 4 in the angular ST-FMR.

orientations can be seen in Figure 4c,d. Both orientations show a clear sin(2ψ) dependance agreeing well with theoretical calculations both qualitatively and quantitatively. Additional angular ST-FMR measurements for (110) and (111) are shown in Figure S9 in the Supporting Information. We find the maximum σ^x_{zx} at 45° to be 130 ± 29 ($\hbar$/e(Ω cm)$^{-1}$) for the (110) orientation and 51 ± 5 ($\hbar$/e(Ω cm)$^{-1}$) for the (111) orientation. Additionally, Figure 4e,f shows the angular dependance of σ^z_{zx} which shows no out-of-plane unconventional SHC within experimental error for the (110) orientation and a cos(ψ) dependance for the (111) orientation with a maximum σ^z_{zx} when current is applied perpendicular to the (1-10) mirror plane with a value of 9 ± 1 ($\hbar$/e(Ω cm)$^{-1}$, agreeing qualitatively with the theoretical calculations.

The experimental results of the unconventional SHCs in our IrO_2 (110) and (111) films qualitatively agree with theoretical predictions using DFT calculations (see the Supporting Information). The unconventional in-plane SHC σ^x_{zx} clearly follows a sin(2ψ) in-plane angular dependance experimentally for both the (110) and (111) orientations which is expected due to the lack of out-of-plane fourfold rotational symmetry. The unconventional out-of-plane SHC σ^z_{zx} clearly follows a cos(ψ) in-plane angular dependance for the (111) orientation and is zero within experimental error for the (110) due to the out-of-plane (110) mirror plane. These results are confirmed for various thicknesses of IrO_2 in the (111) orientation seen in Figure S11 in the Supporting Information. Quantitative differences (see Note S7 in the Supporting Information for quantitative DFT calculations) between theory and experimental are quite common across many material systems such as Pt and IrO_2.[6,28,29] even for conventional SHCs suggesting that there may be something missing in the DFT calculations. We also observe additional field-like torques for the (110) and (111) orientation which we speculate could arise from anisotropic resistance in the ST-FMR devices (see Note S5 and Figure S10, Supporting Information) Interestingly, we do find our unconventional in-plane SHC σ^x_{zx} to match very well with DFT calculations for both (110) and (111) orientations. In addition to the data shown, IrO_2 (111) films undergo lattice distortions induced by the anisotropic epitaxial strain which were characterized using synchrotron X-ray measurements which can be seen in Figure S5 in the Supporting Information. Using these distortions (Note S7, Supporting Information) in our DFT calculations show σ^x_{zx} to be two times larger than what is predicted for bulk IrO_2 (111), agreeing very well with our data shown. These results demonstrate that we can generate and control unconventional SOTs using epitaxial design which can be used as a guide for other material systems that have not been studied in lower symmetry orientations.

3. Conclusion

In summary, we have shown unconventional spin–orbit torques in a high symmetry spin source material, IrO_2, using symmetry design in epitaxial heterostructures. Unconventional torques are not present in high symmetry orientations such as (001) due to vanishing unconventional SHC in the presence of multiple rotational and mirror symmetries of IrO_2 relative to the film growth

direction. In the (110) and (111) orientations, we experimentally observe in-plane unconventional SOTs. Additionally, the (111) orientation shows unconventional out-of-plane SOTs. This is due to the fact that these low symmetry oriented films are only invariant to a small number of symmetry constraints that allows the unconventional SHCs. The unconventional out-of-plane SHC σ^z_{zx} observed in our IrO_2 (111) films are on the same order of magnitude as other low symmetry materials such as noncollinear antiferromagnetic Mn_3GaN and Mn_3Pt, collinear antiferromagnetic RuO_2, and 2D TMD WTe_2,[7,9,10,13] indicating this route to be promising towards finding spintronic materials for PMA switching. This work could provide a route to designing and discovering unconventional spin-torques in other high symmetry materials by using low symmetry orientations. Using this approach, all one needs is a DFT calculation in one orientation for a given material and, using rotation matrices, one can predict unconventional SOTs for lower symmetry orientations.

4. Experimental Section

Sample Growth, Fabrication, and Characterization: Epitaxial IrO_2 was grown on TiO_2 (001), (110), and (111) substrates by RF magnetron sputtering followed by in situ growth of ferromagnetic permalloy $Ni_{81}Fe_{19}$ (Py). The IrO_2 films were grown at 400 °C at a pressure of 30 mTorr with 10% oxygen partial pressure. The target power was 20 W. After growth the sample was cooled in an O_2 atmosphere. Py was then grown in situ at room temperature, 4 mTorr of Ar, power of 35 W, and a background pressure of 3E-7 Torr. The samples were then fabricated using photolithography and ion beam milling, followed by sputter deposition of 100 nm Pt/10 nm Ti and lift off techniques for the electrodes.

Scanning Transmission Electron Microscopy and Strain Analysis: $Py/IrO_2/TiO_2$ interfaces were visualized using STEM (JEM-ARM200F, JEOL) at 200 kV equipped with the aberration corrector (ASCOR, CEOS GmbH). The optimum size of the electron probe was set to be ≈0.7 Å. The collection semiangle of the HAADF detector was ranged from 54 to 216 mrad for clear Z-contrast images. The images were obtained using Smart Align and were conducted on multistacking images and aligned these images using rigid registration to correct for drift and scan distortions. The raw STEM images were filtered to reduce background noise by using Difference Filter (Filters Pro, HREM Research Inc., Japan). STEM samples were prepared by mechanical flat polishing and ion milling process. The polished samples were milled using a 3 keV Ar ion beam. To minimize surface damage, the samples were milled with an acceleration voltage of 100 meV (PIPS II; Gatan, Pleasanton, CA, USA).

ST-FMR Measurements: During the ST-FMR measurements, a microwave current was applied at a fixed frequency (5–12 GHz) and fixed power (10–13 dBm) while sweeping an in-plane magnetic field through the Py resonance conditions from 0 to 0.15 T. The microwave current was modulated at a fixed frequency of 437 Hz and the mixing voltage across the device was measured using a lock-in amplifier. The mixing voltage was fitted versus applied field to extract the symmetric and antisymmetric Lorentzian components. For the angular-dependent ST-FMR, the applied field was rotated in-plane 360° and the symmetric and antisymmetric components were plotted as a function of angle.

Theoretical Calculations: DFT calculations were performed using a Quantum-ESPRESSO code.[30] The plane-wave pseudopotential method with the fully relativistic ultrasoft pseudopotentials[31] was employed in the calculations. The exchange and correlation effects were treated within the generalized gradient approximation (GGA).[32] The plane-wave cut-off energy of 40 Ry and a 16 × 16 × 16 k-point mesh in the irreducible Brillouin zone were used in the calculations. Spin–orbit coupling was included in all the calculations.

The spin Hall conductivity is given by

$$\sigma^k_{ij} = \frac{e^2}{\hbar} \int \frac{d^3\vec{k}}{(2\pi)^3} \sum_n f_{n\vec{k}} \Omega^k_{n,ij}\left(\vec{k}\right) \tag{5}$$

$$\Omega^k_{n,ij}\left(\vec{k}\right) = -2Im \sum_{n\neq n'} \frac{\left\langle n\vec{k}|J^k_i|n'\vec{k}\right\rangle \left\langle n'\vec{k}|v_j|n\vec{k}\right\rangle}{\left(E_{n\vec{k}} - E_{n'\vec{k}}\right)^2} \tag{6}$$

where $f_{n\vec{k}}$ is the Fermi–Dirac distribution for the n-th band, $J^k_i = \frac{1}{2}\{v_i, s_k\}$ is the spin current operator with spin operator s_k and velocity operator $v_j = \frac{1}{\hbar}\frac{\partial H}{\partial k_j}$, and $i, j, k = x, y, z$. $\Omega^k_{n,ij}(\vec{k})$ is the spin Berry curvature in analogy to the ordinary Berry curvature. In order to calculate the spin Hall conductivit, a tight-binding Hamiltonian was constructed using a PAOFLOW code[33,34] that is based on the projection of the pseudo-atomic orbitals (PAO) obtained from the nonself-consistent calculations with a 16 × 16 × 16 k-point mesh. The spin Hall conductivity was calculated using the tight-binding Hamiltonian with a 48 × 48 × 48 k-point mesh by the adaptive broadening method to obtain the converged values. The elements of the spin Hall conductivity tensors for different planes [111], [110] etc. were obtained by transforming the spin Hall conductivity tensor for the [001] plane as follows

$$\sigma^s_{ij,[\text{plane}]} = \sum_{l,m,n} R_{il} R_{jm} R_{kn}\, \sigma^s_{lm,[001]} \tag{7}$$

where R_{il} is an element of the rotation matrix R which transforms from [001] to the desired plane.

Supporting Information

Supporting Information is available from the Wiley Online Library or from the author.

Acknowledgements

This research is supported by Vannevar Bush Faculty Fellowship (ONR N00014-20-1-2844), the Gordon and Betty Moore Foundation's EPiQS Initiative, Grant GBMF9065 to C.B.E. and NSF through the University of Wisconsin MRSEC (DMR-1720415). Transport measurement at the University of Wisconsin–Madison was supported by the US Department of Energy (DOE), Office of Science, Office of Basic Energy Sciences (BES), under award number DE-FG02-06ER46327. Measurements at Cornell were supported by the DOE under award number DE-SC0017671. The authors would also like to thank Maciej Olszewski at Cornell and Neil Campbell at the University of Wisconsin-Madison for discussions regarding magnetic anisotropy in the ST-FMR analysis. The work at UNL was partly supported by the National Science Foundation through the EPSCoR RII Track-1 program (Grant OIA-2044049). STEM measurement at Pohang University of Science and Technology was supported by the Basic Science Research Program through the National Research Foundation of Korea (NRF) funded by the Ministry of Science and ICT (2020R1A4A1018935).

Conflict of Interest

The authors declare no conflict of interest.

Author Contributions

M.P., T.N., and C.B.E. conceived the project. M.P. carried out the thin film growth, device fabrication, and ST-FMR measurements. G.G. and

D.-F.S. performed theoretical calculations. G.N. performed STEM measurments. P.J.R and J.W.K performed synchrotron measurements. J.A.M. and M.M. performed supporting ST-FMR measurements. C.B.E., M.S.R., D.C.R., S.Y.C., and E.Y.T. supervised the study. All authors discussed the results and commented on the manuscript. C.B.E. directed the research.

Data Availability Statement

The data that support the findings of this study are available from the corresponding author upon reasonable request.

Keywords

epitaxial thin films, spin Hall effect, spintronics, unconventional spin–orbit torques

Received: February 19, 2023
Revised: May 27, 2023
Published online: July 20, 2023

[1] L. Liu, C.-F. Pai, Y. Li, H. W. Tseng, D. C. Ralph, R. A. Buhrman, *Science* **2012**, *336*, 555.
[2] C.-F. Pai, L. Liu, Y. Li, H. W. Tseng, D. C. Ralph, R. A. Buhrman, *Appl. Phys. Lett.* **2012**, *101*, 122404.
[3] L. Liu, O. J. Lee, T. J. Gudmundsen, D. C. Ralph, R. A. Buhrman, *Phys. Rev. Lett.* **2012**, *109*, 096602.
[4] S.-H. C. Baek, V. P. Amin, Y.-W. Oh, G. Go, S.-J. Lee, G.-H. Lee, K.-J. Kim, M. D. Stiles, B.-G. Park, K.-J. Lee, *Nat. Mater.* **2018**, *17*, 509.
[5] A. M. Humphries, T. Wang, E. R. J. Edwards, S. R. Allen, J. M. Shaw, H. T. Nembach, J. Q. Xiao, T. J. Silva, X. Fan, *Nat. Commun.* **2017**, *8*, 911.
[6] Y. You, H. Bai, X. Feng, X. Fan, L. Han, X. Zhou, Y. Zhou, R. Zhang, T. Chen, F. Pan, C. Song, *Nat. Commun.* **2021**, *12*, 6524.
[7] H. Bai, X. F. Zhou, H. W. Zhang, W. W. Kong, L. Y. Liao, X. Y. Feng, X. Z. Chen, Y. F. You, Y. J. Zhou, L. Han, W. X. Zhu, F. Pan, X. L. Fan, C. Song, *Phys. Rev. B* **2021**, *104*, 104401.
[8] Y. Liu, Y. Liu, M. Chen, S. Srivastava, P. He, K. L. Teo, T. Phung, S.-H. Yang, H. Yang, *Phys. Rev. Appl.* **2019**, *12*, 64046.
[9] T. Nan, C. X. Quintela, J. Irwin, G. Gurung, D. F. Shao, J. Gibbons, N. Campbell, K. Song, S. Y. Choi, L. Guo, R. D. Johnson, P. Manuel, R. V. Chopdekar, I. Hallsteinsen, T. Tybell, P. J. Ryan, J. W. Kim, Y. Choi, P. G. Radaelli, D. C. Ralph, E. Y. Tsymbal, M. S. Rzchowski, C. B. Eom, *Nat. Commun.* **2020**, *11*, 4671.
[10] A. Bose, N. J. Schreiber, R. Jain, R. Jain, D.-F. Shao, H. P. Nair, J. Sun, X. S. Zhang, D. A. Muller, E. Y. Tsymbal, D. G. Schlom, D. C. Ralph, *Nat. Electron.* **2022**, *5*, 267.
[11] I.-H. Kao, R. Muzzio, H. Zhang, M. Zhu, J. Gobbo, S. Yuan, D. Weber, R. Rao, J. Li, J. H. Edgar, J. E. Goldberger, J. Yan, D. G. Mandrus, J. Hwang, R. Cheng, J. Katoch, S. Singh, *Nat. Mater.* **2022**, *21*, 1029.
[12] S. Shi, J. Li, C. H. Hsu, K. Lee, Y. Wang, L. Yang, J. Wang, Q. Wang, H. Wu, W. Zhang, G. Eda, G. Liang, H. Chang, H. Yang, *Adv. Quantum Technol.* **2021**, *4*, 2100038.
[13] D. MacNeill, G. M. Stiehl, M. H. D. Guimaraes, R. A. Buhrman, J. Park, D. C. Ralph, *Nat. Phys.* **2017**, *13*, 300.
[14] B. Zhao, B. Karpiak, D. Khokhriakov, A. Johansson, A. M. Hoque, X. Xu, Y. Jiang, I. Mertig, S. P. Dash, *Adv. Mater.* **2020**, *32*, 2000818.
[15] M. H. D. Guimarã, G. M. Stiehl, D. Macneill, N. D. Reynolds, D. C. Ralph, *Nano Lett.* **2018**, *18*, 1311.
[16] F. Xue, C. Rohmann, J. Li, V. Amin, P. Haney, *Phys. Rev. B* **2020**, *102*, 14401.
[17] L. Liu, C. Zhou, X. Shu, C. Li, T. Zhao, W. Lin, J. Deng, Q. Xie, S. Chen, J. Zhou, R. Guo, H. Wang, J. Yu, S. Shi, P. Yang, S. Pennycook, A. Manchon, J. Chen, *Nat. Nanotechnol.* **2021**, *16*, 277.
[18] K. Fujiwara, Y. Fukuma, J. Matsuno, H. Idzuchi, Y. Niimi, Y. Otani, H. Takagi, *Nat. Commun.* **2013**, *4*, 2893.
[19] A. Bose, J. N. Nelson, X. S. Zhang, P. Jadaun, R. Jain, D. G. Schlom, D. C. Ralph, D. A. Muller, K. M. Shen, R. A. Buhrman, *ACS Appl. Mater. Interfaces* **2020**, *12*, 55411.
[20] J. N. Nelson, J. P. Ruf, Y. Lee, C. Zeledon, J. K. Kawasaki, S. Moser, C. Jozwiak, E. Rotenberg, A. Bostwick, D. G. Schlom, K. M. Shen, L. Moreschini, *Phys. Rev. Mater.* **2019**, *3*, 64205.
[21] X. Xu, J. Jiang, W. J. Shi, V. Süß, C. Shekhar, S. C. Sun, Y. J. Chen, S. K. Mo, C. Felser, B. H. Yan, H. F. Yang, Z. K. Liu, Y. Sun, L. X. Yang, Y. L. Chen, *Phys. Rev. B* **2019**, *99*, 195106.
[22] Y. Sun, Y. Zhang, C. X. Liu, C. Felser, B. Yan, *Phys. Rev. B* **2017**, *95*, 1.
[23] B. Grover, K. Hazra, T. Ma, B. Pal, N. Bernstein, *Appl. Phys. Lett.* **2022**, *120*, 172406.
[24] T. Ikebuchi, Y. Shiota, T. Ono, *Appl. Phys. Lett.* **2022**, *120*, 072406.
[25] J. Sinova, S. O. Valenzuela, J. Wunderlich, C. H. Back, T. Jungwirth, *Rev. Mod. Phys.* **2015**, *87*, 1213.
[26] L. Liu, T. Moriyama, D. C. Ralph, R. A. Buhrman, *Phys. Rev. Lett.* **2011**, *106*, 036601.
[27] K. Garello, I. M. Miron, C. O. Avci, F. Freimuth, Y. Mokrousov, S. Blügel, S. Auffret, O. Boulle, G. Gaudin, P. Gambardella, *Nat. Nanotechnol.* **2013**, *8*, 587.
[28] L. Zhu, L. Zhu, M. Sui, D. C. Ralph, R. A. Buhrman, *Sci. Adv.* **2019**, *5*, eaav8025.
[29] L. Zhu, R. A. Buhrman, *Phys. Rev. Appl.* **2019**, *10*, 51002.
[30] R. Browning, P. Plachinda, R. Solanki, E. M. Bryant, D. Bayliss, P. Giannozzi, S. Baroni, N. Bonini, M. Calandra, R. Car, C. Cavazzoni, D. Ceresoli, G. L. Chiarotti, M. Cococcioni, I. Dabo, A. Dal Corso, S. De Gironcoli, S. Fabris, G. Fratesi, R. Gebauer, U. Gerstmann, C. Gougoussis, A. Kokalj, M. Lazzeri, L. Martin-Samos, N. Marzari, F. Mauri, R. Mazzarello, S. Paolini, A. Pasquarello, et al., *J Phys Condens Matter* **2009**, *21*, 395502.
[31] D. Vanderbilt, *Phys. Rev. B* **1990**, *41*, 7892.
[32] J. P. Perdew, K. Burke, M. Ernzerhof, *Phys. Rev. Lett.* **1996**, *77*, 3865.
[33] L. A. Agapito, A. Ferretti, A. Calzolari, S. Curtarolo, M. B. Nardelli, *Phys. Rev. B* **2013**, *88*, 165127.
[34] L. A. Agapito, S. Ismail-Beigi, S. Curtarolo, M. Fornari, M. Buongiorno Nardelli, *Phys. Rev. B* **2016**, *93*, 35104.